Hindawi
Shock and Vibration
Volume 2022, Article ID 1781340, 14 pages
https://doi.org/10.1155/2022/1781340

Research Article

Fractional Dimensionless Indicator with Random Forest for Bearing Fault Diagnosis under Variable Speed Conditions

Yujing Huang,[1,2] **Zhi Xu**,[2] **Liang Cao**,[2] **Hao Hu**,[1] **and Gang Tang**[1]

[1]*College of Mechanical and Electrical Engineering, Beijing University of Chemical Technology, Beijing 100029, China*
[2]*Aviation Key Laboratory of Science and Technology on Fault Diagnosis and Health Management, AVIC Shanghai Aero Measurement-Controlling Research Institute, Shanghai 201601, China*

Correspondence should be addressed to Gang Tang; tanggang@mail.buct.edu.cn

Received 15 May 2022; Revised 16 August 2022; Accepted 10 October 2022; Published 19 October 2022

Academic Editor: Arcanjo Lenzi

Fault diagnosis of rolling bearings under variable speed is a common issue in engineering practice, but it lacks an effective diagnosis algorithm, while approaches developed for steady speed cannot be directly applied. Therefore, for effectively identifying bearing faults under variable speed, this paper proposed a multiscale fractional dimensionless indicator (MSFDI) and put forward a fault diagnosis method with random forest (RF). It can overcome the feature space aliasing problem of traditional dimensionless indicators, which will lead to increased diagnosis uncertainty. The multiorder fractional Fourier transform is carried out on bearing signals to get a series of fractional Fourier domain components, which will be used to construct the original MSFDI feature set. Moreover, reliefF selects the sensitive MSFDIs as the input of the RF algorithm to determine the health condition. The effectiveness of the proposed method is verified by experiments and case studies.

1. Introduction

In the aviation system, the engine and transmission system are the most important components. They are not only complex in structure but also have a strong correlation with internal parts [1]. At the same time, the operating environment is very complex. Rolling bearing is one of the key components among them, which is prone to failure and may cause serious chain reactions [2]. Therefore, more and more attention has been paid to the fault diagnosis of aviation bearings [3, 4]. In engineering, due to the influence of starting, stopping, and other working conditions, bearings sometimes run at varying speeds. Therefore, in recent years, bearing fault diagnosis with variable speed has received much attention from academia. Because the signals under variable speed conditions no longer meet the requirements of Fourier transform (FT), the fault diagnosis methods based on the premise of stable speed may not achieve the expected satisfactory results [5]. Therefore, it has become an urgent and valuable task to develop an effective suitable feature extraction and diagnosis method for variable speed.

Vibration signal analysis has extensive applications in rotating machinery fault diagnosis. In order to extract fault features from vibration signals, some kinds of time-frequency analysis methods have been proposed to decompose signals. Wavelet transform (WT) is a classical time-frequency analysis algorithm. Vakharia et al. extracted fault features based on wavelet decomposition to diagnose bearing faults [6]. But it has inevitable energy leakage, and the decomposition effect depends on the wavelet base and decomposition scale [7]. Empirical mode decomposition (EMD) shows the excellent property in dealing with nonstationary signals. Ali et al. used EMD to extract energy entropy as inputs to an artificial neural network, which can automatically detect the severity of bearing failures [8]. However, there are end-effect and mode-mixing problems in EMD [7]. Variational mode decomposition (VMD) can conquer mode mixing, which makes up for the shortcomings of EMD to some extent [9]. Qin et al. developed a redefined dimensionless indicator according to VMD linked with grid search and support vector machine (SVM) [10]. However, such methods are established on the premise of

steady speed operating conditions and need to be combined with computing order tracking (COT) to be used in variable speed conditions, which require synchronous speed information [11]. Fractional Fourier transform (FrFT) extends the frequency domain obtained by using traditional FT to the broader time-frequency domain by adjusting the FrFT rotation angle [12]. The time-frequency information of the variable speed signal can be obtained without synchronous speed information. The main drawback of the FrFT application in fault diagnosis is that it requires expert knowledge, which may lead to deviation. Although the automatic fault diagnosis method combining FrFT and machine learning is more intelligent and effective, there are still few related studies reported.

For fault diagnosis methods with machine learning, the important problem is to extract useful signal features for classification. At present, the commonly used methods usually first decompose a vibration signal through time-frequency analysis methods and combine the features of the time domain, frequency domain, and time-frequency domain to make a multidomain high-dimensional feature set as a basis for subsequent classification. For dimensional indicators, such as root mean square, their magnitudes are related to the absolute amplitude of the signal, that is, related to working conditions [13]. Dimensional indicators under different working conditions are not comparable, so they are not suitable for variable speed conditions. But dimensionless indicators, such as impulse indicators, are not affected by the working state and have relatively stable performance. Therefore, they have extensive application in many research works as fault features [14, 15]. However, the traditional dimensionless indicators often lead to different degrees of aliasing in the feature space, which will increase the diagnosis uncertainty [16]. Xiong et al. pointed out that some dimensionless indicators are highly contradictory because of the indicator overlap between different faults [17]. For instance, the dimensionless indicators for shaft bending and bearing inner race fault range little difference. Qin et al. also showed that dimensionless indicators would bring uncertainty in fault diagnosis results [15]. The indicator curves from the different concurrent faults overlay one another. In addition, due to the nonstationarity of the signal, the analysis of dimensionless indicators at the first scale may produce unreliable results [16]. Therefore, this paper proposes a multiscale fractional dimensionless indicator (MSFDI), in which FrFT is used to provide multidomain representations, and the multiscale method brings richer features while solving aliasing in the feature space. In other words, MSFDI can reflect the stable fault information of multidomain vibration signals at different scales.

The high-dimensional MSFDI feature set not only displays the inherent characteristics of the signal extensively but also brings some redundant or negative feature information and higher calculation cost. To improve the classification accuracy while reducing the calculation cost, feature selection should be performed to get the most informative fault features for classification so as to classify with a low-dimensional sensitive feature subset. Common feature selection algorithms include the filter type and wrapper type. The former ones, such as ReliefF [6], the Pearson correlation coefficient (PCC) [18], and neighborhood component analysis (NCA) [19], are screened according to the importance of the features. The latter, such as manta ray foraging optimization (MRFO) [20], equilibrium optimizer (EO) [21], slim mold algorithm (SMA) [22], generalized normal distribution optimization (GNDO) [23], and marine predators algorithm (MPA) [24], regards feature subset selection as a search optimization problem and can select the best feature subset for a specific classification model.

Based on the constructed fault features, scholars have developed many useful fault classification methods, such as AdaBoost [25], BP neural network (BPNN) [26], discriminant analysis (DA) [27], decision tree (DT) [28], Gaussian mixture model (GMM) [29], K-nearest neighbour (KNN) [30], naive Bayes (NB) [19], random forest (RF) [31], support vector machine (SVM) [32], and others. Liu et al. adopted the AdaBoost combined binary classifier and applied it to the fault multiclassification problem [25]. Li et al. combined BPNN with multiscale local features for diagnosis [26]. Cao et al. used GMM to classify crack faults [29]. Cui et al. proposed a bearing fault diagnosis framework and selected NB as the diagnosis model [19]. Tang et al. proposed a particle swarm optimization RF classifier [31]. The simple implementation, fast training speed, and excellent classification capabilities of RF make it stand out among many machine learning-classification methods. In addition, deep learning models without feature engineering are also developing rapidly [33, 34]. However, in the aviation field, according to the guidance for vibration-based diagnostic algorithms, computational efficiency and physical description are emphasized. Due to the black-box effect and slow running speed, deep-learning models are not considered in this paper.

According to the above discussions, for accurately extracting fault features and correctly diagnosing fault categories with variable speeds, this paper develops a fault diagnosis method on the basis of MSFDI and RF. First, the multiorder FrFT is performed on the collected bearing signals of different health and speed-changing conditions to obtain a series of fractional Fourier domain (FrFD) components. Based on these components, MSFDI is calculated to build a high-dimensional feature set. Then, ReliefF is used to select an RF feature subset, which is more sensitive for classification, and as the input of the RF, the algorithm determines the health condition.

The main contributions are summarized as follows:

(1) The developed method can be applied to bearing fault diagnosis with variable speed but without additional synchronous speed information. By adjusting the FrFT rotation angle, it can realize signal representation in any time-frequency domain.

(2) The proposed MSFDI can extract the dimensionless indicator on different FrFD and different scales, which overcomes the aliasing problem of the traditional dimensionless indicator in feature space, and provides more useful information for bearing fault classification.

2. Basic Theory

2.1. Fractional Fourier Transform (FrFT). Fractional Fourier transform (FrFT) extends the frequency domain obtained by using traditional FT to a more generalized fractional Fourier domain (FrFD). Similar to that, FT can be regarded as the representation in the frequency-axis obtained by $\pi/2$ counterclockwise rotation of the time-axis. FrFT can be regarded as the representation in the corresponding FrFD, which can be obtained by any angle of counterclockwise rotation of the time-axis [35].

The p th-order FrFT of the signal $x(t)$ can be expressed as $X_p(t)$ or $F^p x(t)$, that is, [36]

$$X_p(u) = F^p x(t) = \int_{-\infty}^{+\infty} x(t) K_p(u,t) 0t, \tag{1}$$

where F^p is the FrFT operator, and $K_p(u,t)$ is the transformation kernel.

$$K_p(u,t) = \begin{cases} A_\alpha \exp\left(j\pi\left(t^2 \cot\alpha + u^2 \cot\alpha - 2tucsc\alpha\right)\right), \alpha \neq n\pi, \\ \delta(u-t), \alpha = 2n\pi, \\ \delta(u+t), \alpha = (2n \pm 1)\pi, \end{cases} \tag{2}$$

where $A_\alpha = \sqrt{1 - jcot\alpha}$, p is the FrFT order, α is the corresponding rotation angle with corresponding, and n is an integer.

With the increase of the FrFT order from 0 to 1, $X_p(t)$ gradually changes from the time domain to the frequency domain. When $p = 0$, $X_0(u) = x(t)$. When $p = 1$, $X_1(u) = \int_{-\infty}^{+\infty} e^{-j2\pi ut} x(t) 0t$ is the FT of $x(t)$.

FrFT contains time-frequency domain information, and with changes of FrFT order p, it can represent the time-frequency domain generated by rotation change from the time domain to the frequency domain, carrying different feature information. Figure 1(a) shows coordinate rotation corresponding to FrFT, where (t, f) is the normal time-frequency plane and (u, v) is the fractional domain plane. Figures 1(b)–1(d) show the representation of the same signal in different FrFDs.

2.2. Dimensionless Indicator. In practice, the dimensional indicator varies under different working conditions, so they are easily influenced by load, speed, and so on. However, dimensionless indicators are sensitive to faults. Their performance is relatively stable and not affected by working conditions. So, dimensionless indicators are used as diagnosis features extensively.

Traditional dimensionless indicators can be expressed as [17]

$$\zeta_x = \frac{\left[\int_{-\infty}^{+\infty} |x|^n p(x) dx\right]^{1/n}}{\left[\int_{-\infty}^{+\infty} |x|^m p(x) dx\right]^{1/m}}, \tag{3}$$

where x is the signal amplitude, and $p(x)$ is the probability density function (PDF) of the signal amplitude.

If n = 2, m = 1, the waveform indicator is obtained

If $n \longrightarrow \infty$, $m = 1$, the impulse indicator is obtained

If $n \longrightarrow \infty$, $m = 1/2$, the margin indicator is obtained

If $n \longrightarrow \infty$, $m = 2$, the peak indicator is obtained

The kurtosis indicator is $K = \int_{-\infty}^{+\infty} x^4 p(x) dx / X_{rms}^4$, where $X_{rms} = \sqrt{\int_{-\infty}^{+\infty} x^2 p(x) dx}$.

The skewness indicator is $S = \int_{-\infty}^{+\infty} x^3 p(x) dx / X_{rms}^3$.

It can be seen that the dimensionless indicator is almost not limited by the amplitude and frequency of the signal and is mainly related to the curve of the PDF.

2.3. ReliefF. ReliefF is a filter-type feature selection algorithm. According to category relevance, each feature will be assigned a weight to represent its contribution to classification. The feature with a lower weight than the preset threshold will be cut out [37].

ReliefF firstly chooses a random sample Rn from the original dataset, then k samples from the identical category and different categories of Rn are randomly selected, respectively. The distances of feature A between the same class and different classes are calculated separately. If there is a large difference between the average distances of the two classes, it means that this feature has better discrimination ability for this class, and the weight of this feature is increased; otherwise, it means that there is no discrimination ability, and the weight of this feature is reduced. These operations are repeated m times for each feature, and the weight values of each feature are calculated. (4) is used for updating the weights as follows:

$$W(A) = W(A) - \frac{\sum_{j=1}^{k} \mathrm{diff}\left(A, R, H_j\right)}{mk} + \frac{\sum_{C \notin class(R)} \left[p(C)/1 - p(class(R)) \sum_{j=1}^{k} \mathrm{diff}\left(A, R, M_j(C)\right)\right]}{mk}, \tag{4}$$

where $W(A)$ is the weight of feature A; $p(C)$ is the proportion of samples with C-class in the original data set; H_j is the j^{th} sample from an identical class variable and nearest to sample R; $M_j(C)$ is the j^{th} sample from a different class variable and nearest to sample R. $\mathrm{diff}(A, R_1, R_2)$ is the Euclidean distance between samples R_1 and R_2, which can be calculated by

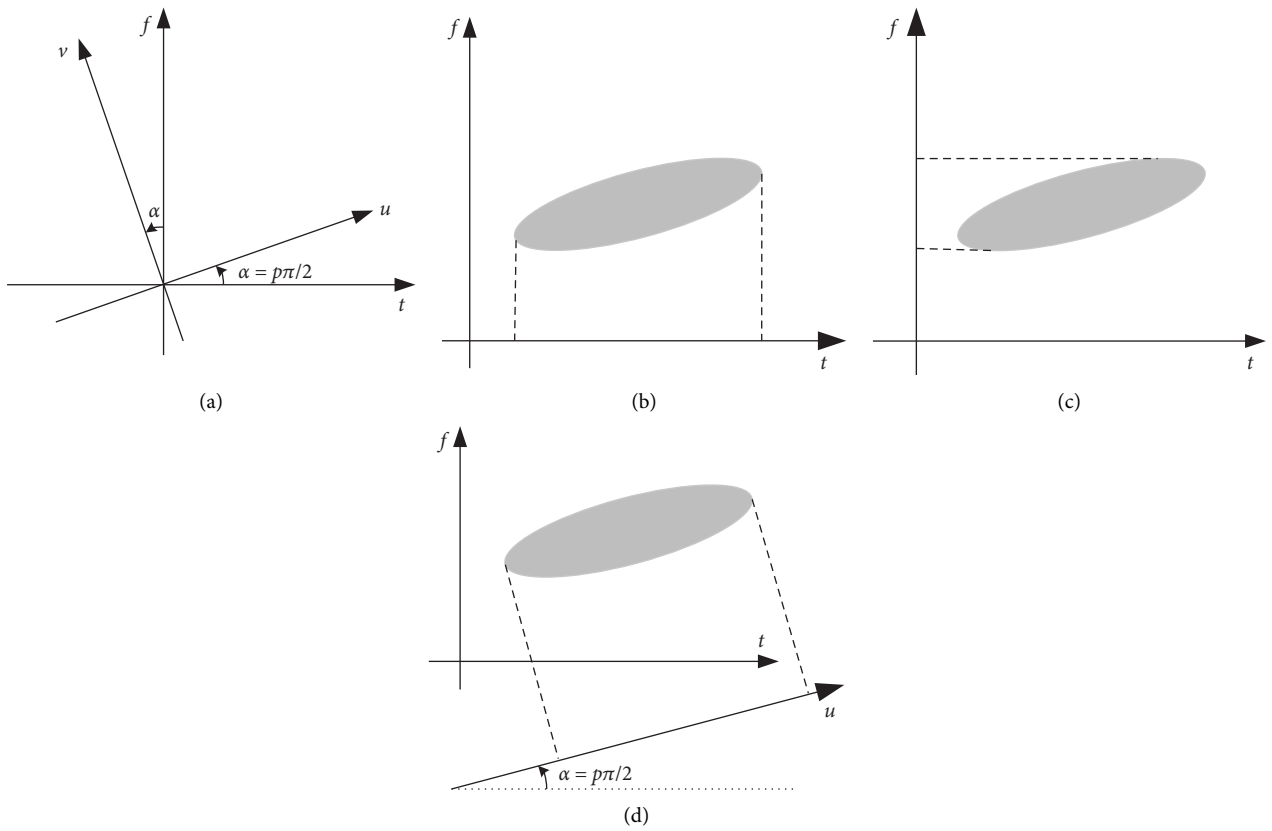

Figure 1: FrFT-related representations: (a) coordinate rotation; (b) time-domain representation ($p = 0$); (c) frequency-domain representation ($p = 1$); (d) FrFD representation (random p).

$$\mathrm{diff}\left(A, R_1, R_2\right) = \begin{cases} \dfrac{\left|R_1[A] - R_2[A]\right|}{\max(A) - \min\ (\mathrm{A})}, \text{if A is continues,} \\ 0, \text{if A is continues an } \mathrm{d}R_1[A] = R_2[A], \\ 1, \text{if A is continues an } \mathrm{d}R_1[A] \neq R_2[A]. \end{cases} \tag{5}$$

$W = \{w_1, w_2, \cdots, w_n\}$ is the final feature weight vector, sorting the features according to the weight from high to low. Features with higher weights than the preset weight threshold are set as sensitive ones.

3. The Proposed Method

3.1. Multiscale Fractional Dimensionless Indicator (MSFDI). Considering that there are many types of bearing faults, more useful fault information needs to be extracted from the vibration signal to distinguish more fault types. So, this paper developed a multiscale fractional dimensionless indicator (MSFDI). MSFDI means to the dimensionless indicators calculated on a set of FrFD components with different scales through a coarse-grain process, which overcomes the different degrees of aliasing of traditional dimensionless indicators in the feature space, and provides more information about the health status of bearings.

For a signal $S = \{x_1, x_2, \cdots, x_n\}$, according to the order of FrFT $p \in [0, 0.1, \cdots, 1]$, the corresponding FrFT is proposed to the original signal S to obtain 11 FrFD components $\{S_0, S_{0.1}, \cdots, S_1\}$, in which S_0 is time domain representation and S_1 is frequency domain representation.

For any FrFD component $S_p = \left\{x_{p,1}, x_{p,2}, \cdots, x_{p,n}\right\}$, it is divided by τ-length window without overlapping. Vector $\left\{x_{p,(j-1)\tau+1}, x_{p,(j-1)\tau+2}, \cdots, x_{p,j\tau}\right\}$ $(1 \le j \le n/\tau)$ with τ-length is in the j^{th} window. As shown in Figure 2, the coarse-grained data series $y_p^{(\tau)} = \left\{y_{p,1}^{(\tau)}, y_{p,2}^{(\tau)}, \cdots, y_{p,j}^{(\tau)}\right\}$ $(1 \le j \le n/\tau)$ is constructed with the following equation:

$$y_{p,j}^{(\tau)} = \frac{1}{\tau} \sum_{i=(j-1)\tau+1}^{j\tau} x_{p,i}, 1 \le j \le \frac{n}{\tau}, \tag{6}$$

where τ is scale factor, and the data inside each window are averaged [38].

The dimensionless indicator calculated based on each coarse-grained data series is called MSFDI. Before calculating MSFDI, it is necessary to explore the availability of dimensionless indicators in FrFD. From Section 2.2, it is clear that the dimensionless indicator is almost not limited by the amplitude and frequency of the signal and is only related to the curve of the PDF. Signals from a health bearing and an inner race fault bearing with acceleration conditions, which are from the University of Ottawa, are chosen to prove the availability of dimensionless indicators in FrFD [39].

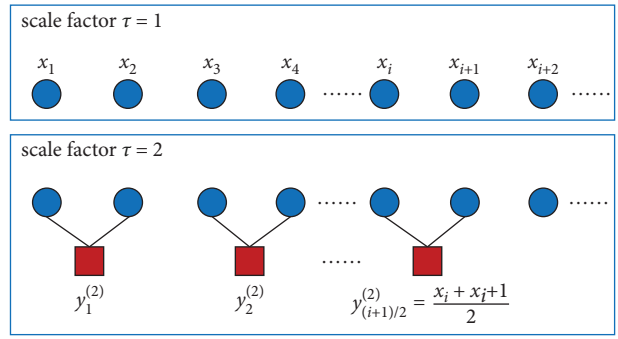

Figure 2: Schematic illustration of the coarse-grained procedure.

Taking the order of FrFT $p \in [0, 0.3, 0.6, 1]$ as an example, Figure 3 shows the PDF curves of $\{S_0, S_{0.1}, S_{0.6}, S_1\}$ obtained by the health and fault signals, respectively, in which the healthy one is marked in blue and the faulty one is marked in red. It can be clearly seen that at different orders of FrFT, the PDF curves of the health and fault-bearing signals show significant differences. Therefore, it can be considered that the dimensionless indicators have the ability to diagnose faults in FrFD.

According to the theories and analysis above, MSFDI including six categories is defined as follows:

$$
\begin{aligned}
MSFDI_W &= \frac{\left[\int_{-\infty}^{+\infty} \left|y_p^{(\tau)}\right|^2 p\left(y_p^{(\tau)}\right) dy_p^{(\tau)}\right]^{1/2}}{\int_{-\infty}^{+\infty} \left|y_p^{(\tau)}\right| p\left(y_p^{(\tau)}\right) dy_p^{(\tau)}},\\
MSFDI_I &= \lim_{l \longrightarrow \infty} \frac{\left[\int_{-\infty}^{+\infty} \left|y_p^{(\tau)}\right|^l p\left(y_p^{(\tau)}\right) dy_p^{(\tau)}\right]^{1/l}}{\int_{-\infty}^{+\infty} \left|y_p^{(\tau)}\right| p\left(y_p^{(\tau)}\right) dy_p^{(\tau)}},\\
MSFDI_M &= \lim_{l \longrightarrow \infty} \frac{\left[\int_{-\infty}^{+\infty} \left|y_p^{(\tau)}\right|^l p\left(y_p^{(\tau)}\right) dy_p^{(\tau)}\right]^{1/l}}{\left[\int_{-\infty}^{+\infty} \left|y_p^{(\tau)}\right|^{1/2} p\left(y_p^{(\tau)}\right) dy_p^{(\tau)}\right]^2},\\
MSFDI_P &= \lim_{l \longrightarrow \infty} \frac{\left[\int_{-\infty}^{+\infty} \left|y_p^{(\tau)}\right|^l p\left(y_p^{(\tau)}\right) dy_p^{(\tau)}\right]^{1/l}}{\left[\int_{-\infty}^{+\infty} \left|y_p^{(\tau)}\right|^2 p\left(y_p^{(\tau)}\right) dy_p^{(\tau)}\right]^{1/2}},\\
MSFDI_K &= \frac{\int_{-\infty}^{+\infty} \left|y_p^{(\tau)}\right|^4 p\left(y_p^{(\tau)}\right) dy_p^{(\tau)}}{\left(\int_{-\infty}^{+\infty} \left|y_p^{(\tau)}\right|^2 p\left(y_p^{(\tau)}\right) dy_p^{(\tau)}\right)^2},\\
MSFDI_S &= \frac{\int_{-\infty}^{+\infty} \left|y_p^{(\tau)}\right|^3 p\left(y_p^{(\tau)}\right) dy_p^{(\tau)}}{\left(\int_{-\infty}^{+\infty} \left|y_p^{(\tau)}\right|^2 p\left(y_p^{(\tau)}\right) dy_p^{(\tau)}\right)^{3/2}},
\end{aligned}
\tag{7}
$$

where $y_p^{(\tau)}$ denotes the coarse-grained series of p-order FrFD component of the signal and $p(y_p^{(\tau)})$ denotes the corresponding PDF.

3.2. Bearing Fault Diagnosis under Variable Speed Conditions with MSFDI. To achieve effective bearing fault feature extraction and accurate diagnosis with variable speeds, combined with the basic theories above, this paper presents a new feature, MSFDI of vibration signals, and realizes intelligent fault diagnosis by combining the RF algorithm. Figure 4 is the flow chart of this method, and the specific process is described in the following figure:

3.2.1. FrFT Processing of the Vibration Signals. The FrFT order p can be chosen from $[0, 0.1, \cdots, 1]$. The FrFT with the corresponding orders are performed on the original vibration signal to obtain a series of FrFD components $\{S_0, S_{0.1}, \cdots, S_1\}$, in which S_0 is the time domain representation, i.e., the original vibration signal, S_1 is the frequency domain representation, and the other 9 FrFD components correspond to different time-frequency domain representations of the original signal.

3.2.2. Fault Feature Extraction of MSFDI. Based on the 11 FrFD components obtained in the first step, six types of MSFDIs of different scales are extracted as an original feature set for classification, namely, $MSFDI_W$, $MSFDI_I$, $MSFDI_M$, $MSFDI_P$, $MSFDI_K$, and $MSFDI_S$. In this paper, the maximum scale factor $\tau = 10$. Therefore, a high-dimensional feature matrix including $6 \times 11 \times 10$ MSFDIs is constituted, which is

$$
V = \left[MSFDI_{W\,p,\tau}, MSFDI_{I\,p,\tau}, MSFDI_{M\,p,\tau}, MSFDI_{P\,p,\tau}, MSFDI_{K\,p,\tau}, MSFDI_{S\,p,\tau}\right], \tag{8}
$$

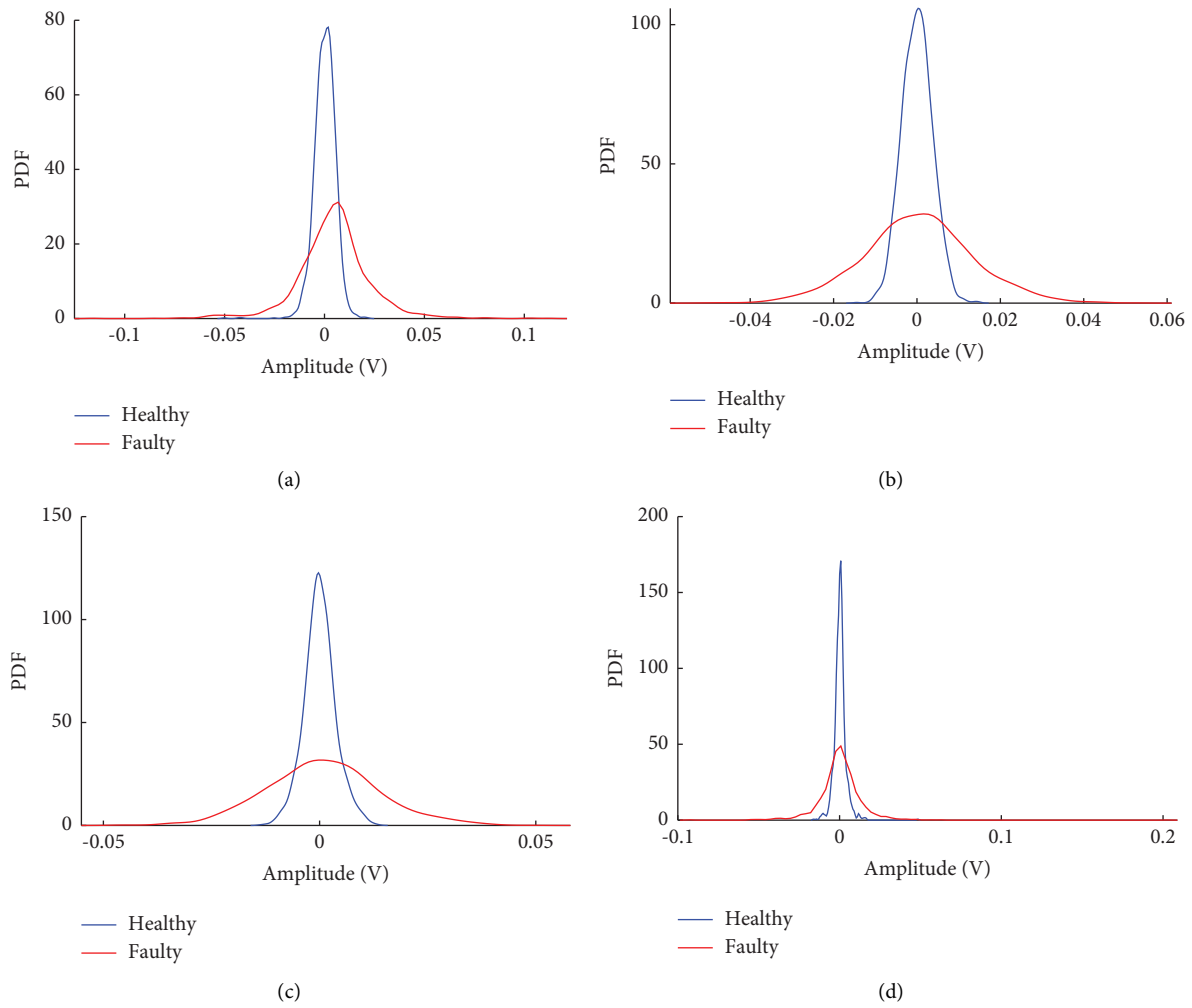

Figure 3: PDF curves of the health and fault signals: (a) $p = 0$; (b) $p = 0.3$; (c) $p = 0.6$; (d) $p = 1$.

where $p = 0, 0.1, \cdots, 1$ and $\tau = 1, 2, \cdots, 10$. These MSFDIs include different angles of time-frequency domain features at different scales and can fully reflect the fault information contained in the vibration signal.

3.2.3. Fault Feature Evaluation and Selection with ReliefF. Different MSFDIs have different sensitivities to health conditions. The high-dimensional feature matrix can add effective fault diagnosis information but bring redundancy and negative information as well, which may not only cut down recognition accuracy but also raise the calculation cost. Therefore, this paper selects MSFDI with high sensitivity through the feature evaluation method. Specifically, the ReliefF algorithm is used to evaluate MSFDI in this study, which gives higher weights to features with high correlation with health conditions, and all MSFDIs are sorted according to the final feature weight vector. This paper sets the weight threshold to 0, and the features with weights above the threshold are chosen as sensitive MSFDIs to form an RF feature subset, which will be used in the next classification algorithm.

3.2.4. RF Classification to Identify Health Conditions. Vibration signals are collected on the bearing test rig under different variable speed conditions, which are divided into the training set and the test set. The testing set is input to the RF trained by the training set, the results of all decision trees in the RF are summarized, and the result by the majority voting is set as the output of the RF. The health status of the bearing can be determined according to the output of the RF classifier.

4. Experiment

Vibration signals bearing different health conditions from the University of Ottawa are used to validate the proposed method, which is collected under time-variable rotational speed conditions [39]. The test rig is shown in Figure 5. Both sides of the rotating shaft are supported by using two rolling bearings. The left side is the healthy bearing, and the right side is the experimental one, which will be with different health conditions during the experiment [39]. Vibration signal samples in the following four health states are collected: health (CH), inner-race fault (CI), outer-race fault (CO), and ball fault (CB), which are collected under four

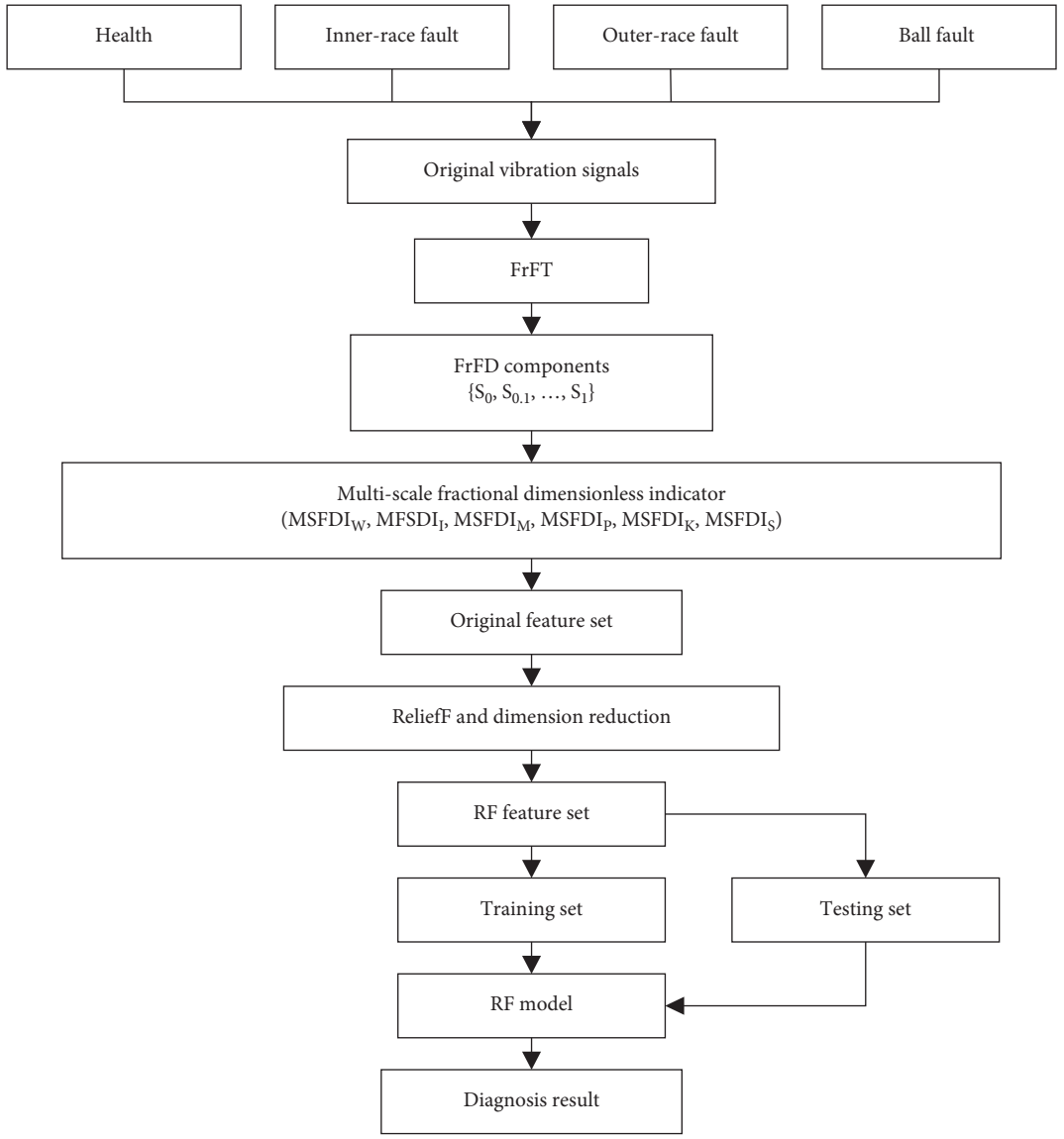

Figure 4: Flow chart of this method.

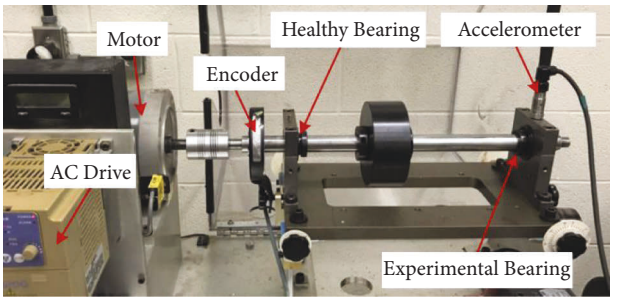

Figure 5: Test rig [26].

variable speed conditions: speed-up, speed-down, speed-up then speed-down, and speed-down then speed-up.

The sampling frequency of the vibration signals is 200 kHz, and the signal is down-sampled by a factor of 10 to reduce the calculation [40]. By performing nonoverlapping division of samples with a window of 0.1 s, 100 samples are obtained in each health condition under each speed condition, so each health condition is arranged with 400 sets of

vibration data with different variable speeds. Random 280 sets of vibration samples under each health condition are set as training data. The left 120 sets serve as test data.

Figure 6 is the time-domain waveform of the signals under four health conditions. It can be observed that although CI, CO, and CB correspond to different fault conditions, their time domain waveforms are not much different, and only the waveform corresponding to CI is significantly different, with obvious fault pulses. Therefore, the new-raised method is used to mine the hidden features behind the signals.

A series of FrFT processing is performed on the original vibration signals of the aforementioned four health conditions: CH, CI, CO, and CB. As mentioned earlier, the order of FrFT $p \in [0, 0.1, \cdots, 1]$, and each sample signal is transformed to get 11 FrFD components $\{S_0, S_{0.1}, \cdots, S_1\}$, which show the signal representations in time-frequency space. Each FrFD component is processed through multiscale analysis to obtain coarse-grained series at different scales, and $\tau_{\max} = 10$. The corresponding MSFDIs are calculated by using the coarse-grained series with different scale factors. Through the analysis above, the high-dimensional original feature set can be obtained, containing 660 MSFDIs in total. On the one hand, it brings a huge amount of calculation. On the other hand, it contains some features that are not conducive to classification and affect the classification effect. Taking MSFDIW as an example, Figure 7 shows the classification effectiveness of four MSFDIW with different FrFT orders and scale factors. The horizontal axis shows the sample number, and the vertical axis shows the MSFDIW value. Sample numbers 1–400, 401–800, 801–1200, and 1201–1600 represent the health states CH, CI, CO, and CB, respectively. The classification effectiveness depends on the overlap degree of MSFDIW of the four health states. The lower the overlap degree, the higher the classification effectiveness of the feature. In Figures 7(a) and 7(b), the overlap degree of corresponding MSFDIW is low, especially for the health state CI, which has almost no overlap with the other three states, which shows that $MSFDI_{W0,1}$ and $MSFDI_{W0.9,1}$ have good classification effectiveness. By contrast, the corresponding MSFDIW in Figures 7(c) and 7(d) has a large overlap, especially for Figure 7(d), the four health states are completely overlapped, which shows the difficulty of effective classification based on $MSFDI_{W0.8,4}$ and $MSFDI_{W0.5,7}$.

Since the sensitivity of each MSFDI has a direct impact on the diagnostic outcome, the ReliefF algorithm was used to assess the classification performance of MSFDI. ReliefF assigns higher weights to features with a high correlation with health status to select features with better performance from many MSFDIs. Figure 8 shows the weights of the original feature set, where the horizontal and vertical axes are the MSFDI number and the corresponding weight value, respectively. The specific order of the original feature set is as follows: the first 66 MSFDIs are at scale 1, among which the first 6 MSFDIs are for the FrFD component S_0, the next 6 MSFDIs are for the FrFD component $S_{0.1}$, and so on; the last 6 MSFDIs are for the FrFD component S_1. The next 66 MSFDIs are at scale 2, in the same way up to the last scale 10.

In this paper, the weight threshold is set as 0 as a measure of MSFDIs' sensitivity to classification, and the features with higher weights than the threshold are selected as the sensitive MSFDIs. Thus, 57 MSFDIs with weight values greater than 0 are selected as RF feature subsets to reduce the cost of subsequent calculation. The RF classifier is applied to identify four bearing health conditions. The numbers of decision trees and nodes are important parameters of RF. In the model, Bayesian optimization is used to obtain the optimal parameters. Table 1 compares the results with ReliefF or not in terms of feature number and accuracy. It can be summarized that the new-raised method has fewer features and higher classification accuracy. Figure 9(a) is the classification result of the original feature set without feature selection, and Figure 9(b) is the result of the RF feature set selected by ReliefF. The horizontal axis is the health condition label obtained by the classification model, the vertical axis is the real label of the sample, and the diagonal line is the classification accuracy of each health state, which has the same meaning in the following figure. The comparison proves the effectiveness of this method.

5. Comparison

5.1. Comparison of Feature Extraction Methods. To show the superiority of MSFDI, it is compared with other fault feature extraction methods. Figure 10(a) is the classification result of the traditional dimensionless with $p = 0$ and $\tau = 1$, and each sample corresponds to 6 features. Figure 10(b) is the final classification accuracy of the dimensionless indicators of the 11 FrFD components ($p \in [0, 0.1, \cdots, 1]$) with a scale factor $\tau = 1$, and each sample corresponds to 66 features. Figure 10(c) is the final classification accuracy of the dimensionless indicators of the time domain signal ($p = 0$) with a scale factor $\tau \in [1, 2, \cdots, 10]$, and each sample corresponds to 60 features.

Since the number of the above three input features is almost the same as that in the proposed method, all the features are taken as the input. The average classification accuracy of the above three methods is 73.75%, 90.83%, and 80.63%, which are better than the compared methods with traditional dimensionless indicators. The result with multi-FrFD (Figure 10(b)) is better than that with multiscale (Figure 10(c)), indicating that the former can provide better fault information. By contrast, as shown in Figure 9(b), the proposed method selects sensitive MSFDIs based on a combination of multi-FrFD and multiscale, which effectively improves the diagnostic accuracy to 97.92%.

5.2. Comparison of Feature Selection Methods. To verify that ReliefF performs well in sensitive MSFDI selection, 7 algorithms including PCC [18], NCA [19], MRFO [20], EO [21], SMA [22], GNDO [23], and MPA [24] were selected to evaluate all 660 MSFDIs. Among them, PCC, NCA, and ReliefF all belong to filter feature selection. In order to avoid the influence of feature quantity on classification performance, these algorithms also select the first 57 features with greater importance. The remaining 5 algorithms are selected

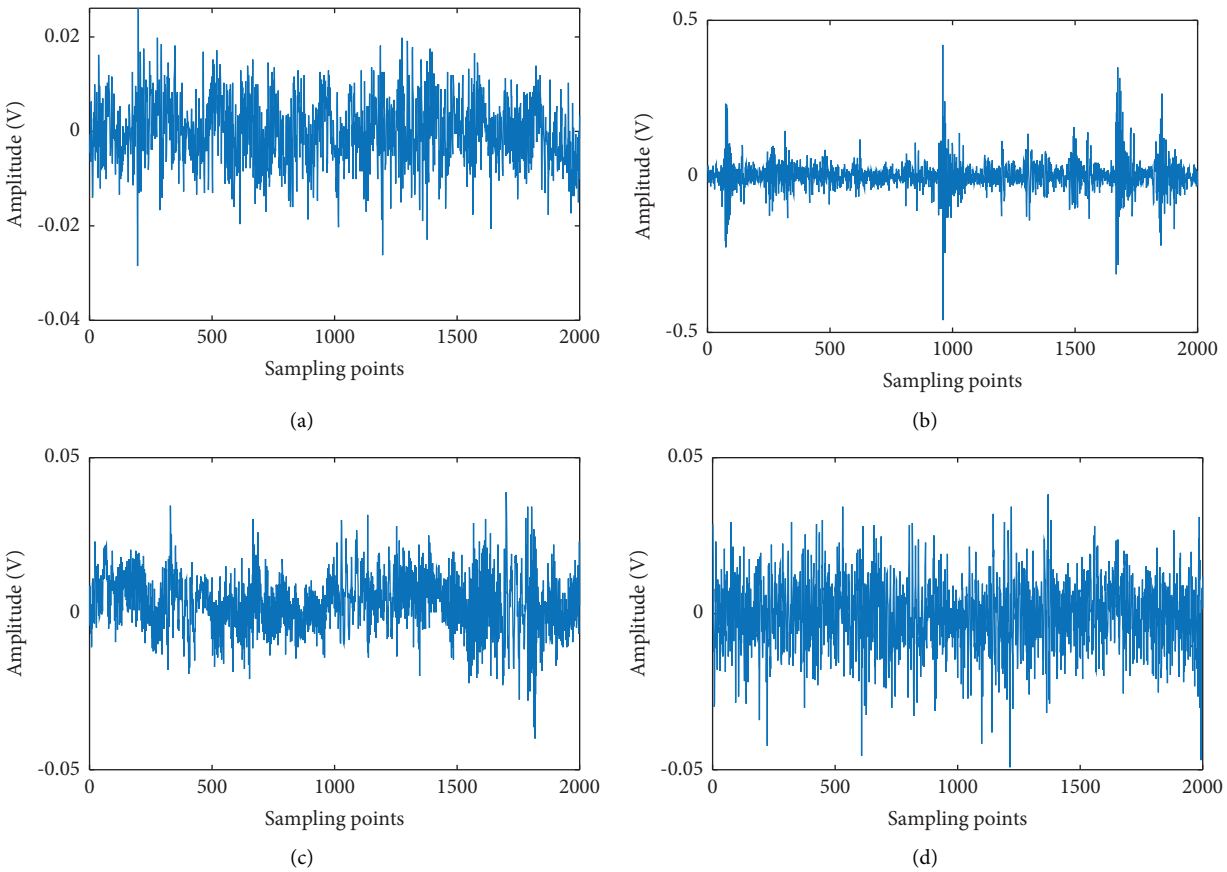

Figure 6: Time-domain waveforms: (a) CH; (b) CI; (c) CO; (d) CB.

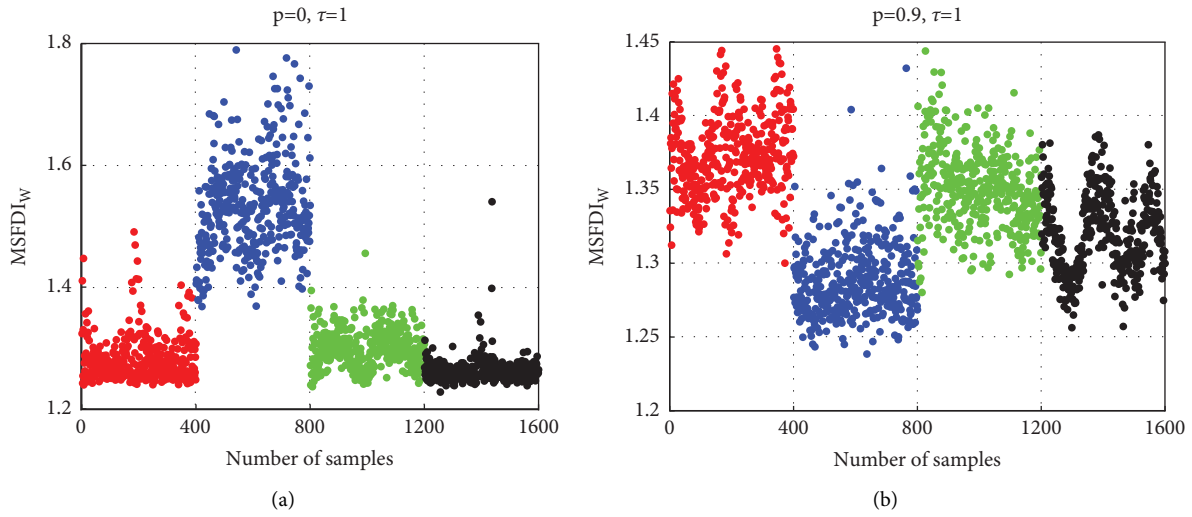

Figure 7: Continued.

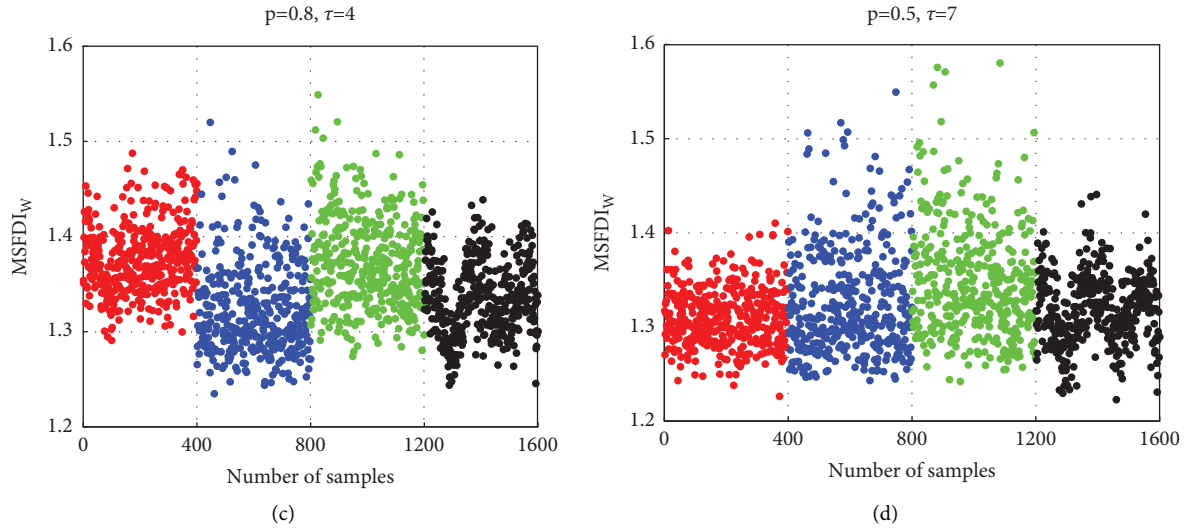

Figure 7: $MSFDI_W$ with different orders of FrFT p and scale factor τ: (a) $p = 0$, $\tau = 1$; (b) $p = 0.9$, $\tau = 1$; (c) $p = 0.8$, $\tau = 4$; (d) $p = 0.5$, $\tau = 7$.

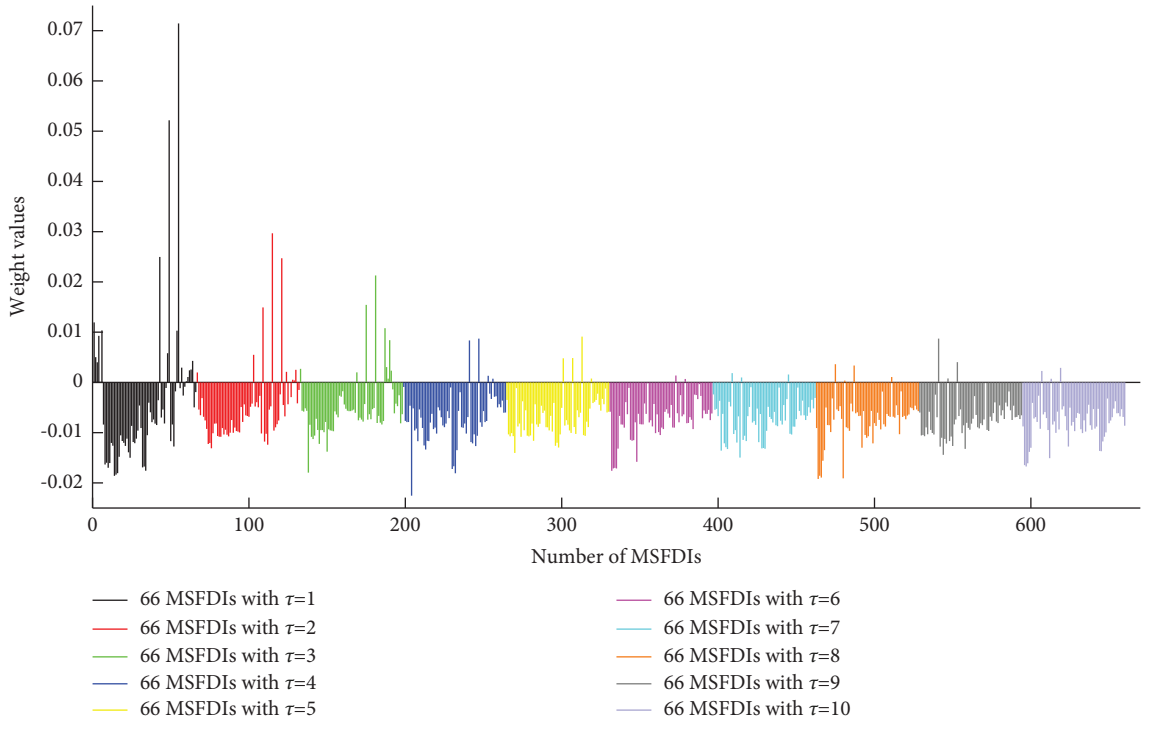

Figure 8: The weights of the original feature set.

Table 1: Comparison of results with reliefF or not.

	Feature number	Accuracy (%)
Method without ReliefF	660	95.42
The proposed method	57	97.92

by using the wrapper algorithm, and the number of selected features varies according to the algorithm.

Table 2 is the classification accuracy comparison of feature selection algorithms. It can be seen that the ReliefF algorithm in this paper is only inferior to MAP in the CB classification accuracy, and the classification accuracies of the remaining four aspects are the highest. In addition, among all feature selection methods, the CI

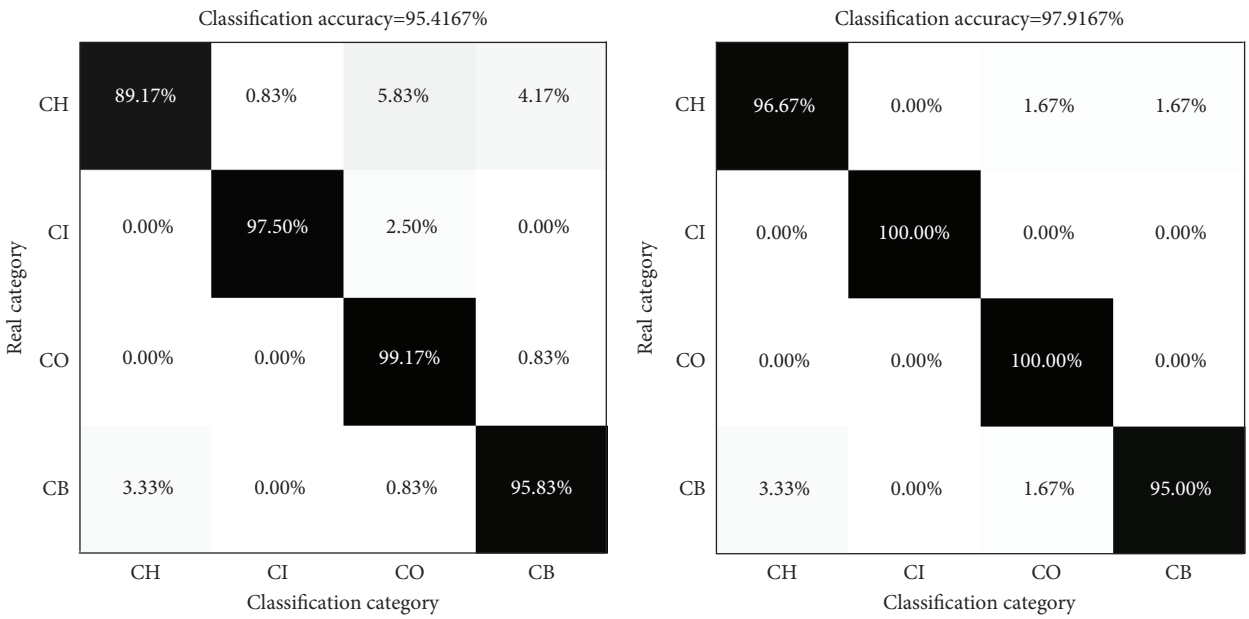

Figure 9: The classification results of (a) the original feature set; (b) the RF feature set (the proposed method).

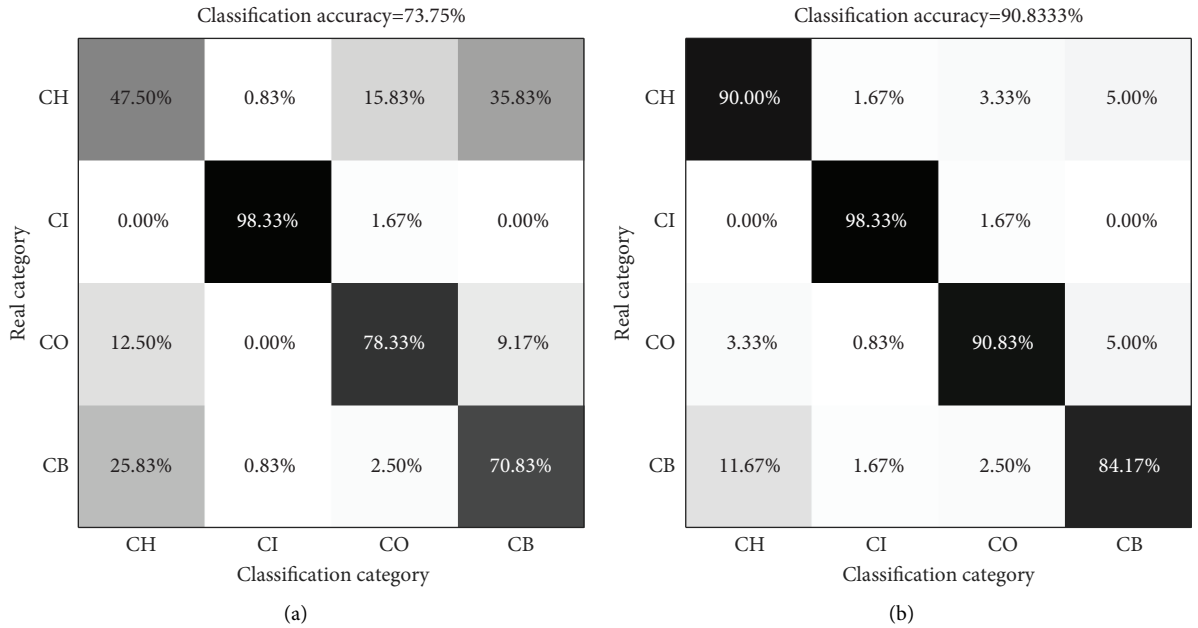

Figure 10: Continued.

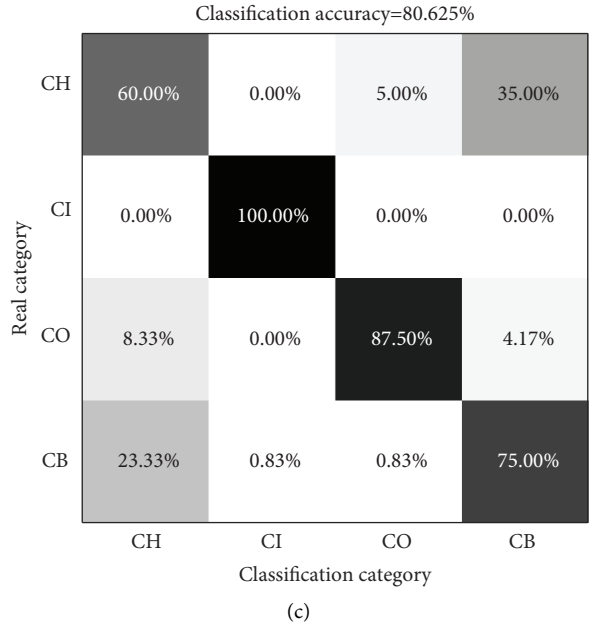

(c)

Figure 10: Comparison of feature extraction methods: (a) traditional dimensionless indicators ($p = 0$, $\tau = 1$); (b) dimensionless indicators with multi-FrFD ($p \in [0, 0.1, \cdots, 1]$, $\tau = 1$); (c) dimensionless indicators with multiscale ($p = 0$, $\tau \in [1, 2, \cdots, 10]$).

Table 2: Comparison of feature selection methods.

	CH accuracy (%)	CI accuracy (%)	CO accuracy (%)	CB accuracy (%)	Overall accuracy (%)
ReliefF (in this paper)	**96.67**	**100**	**100**	95	**97.92**
PCC	91.67	100	95.83	94.17	95.42
NCA	80.83	94.17	96.67	89.17	90.21
MRFO	89.17	95.83	95.83	89.17	92.50
EO	90.83	97.50	99.17	89.17	94.17
SMA	85.83	93.33	91.67	94.17	91.25
GNDO	87.50	99.17	96.67	96.67	95
MPA	93.33	96.67	95	**98.33**	95.84

classification accuracy is always the highest, which is also consistent with the information reflected in Figure 6(b) that is, the fault pulse in the CI signal is more obvious and conducive to classification. The comparison proves that the ReliefF method performs best on sensitive MSFDI selection.

5.3. Comparison of Classifiers. In addition, to demonstrate the advantages of the RF classifier in the newly proposed method, 9 other common classifiers, AdaBoost [25], BPNN [26], DA [27], DT [28], GNN [29], KNN [30], NB [19], SVM [32], and CNN [33], are selected for comparison. In all classification models, the parameter optimization method is the same as RF, using Bayesian optimization, trying to minimize the cross-validation error for classification algorithms by varying the parameters. For fairness, these methods are classified with 57 sensitive MSFDIs selected by ReliefF, which are the same as the proposed method. For CNN, the original vibration signal is used as the additional input of CNN.

Table 3 is the classification accuracy comparison of classifier models. It can be seen that the RF model in this paper is only a little inferior to CNN (with original vibration signal) in the CH and CB classification accuracy, and the classification accuracies of the remaining three aspects are the highest. In addition, the RF model reduces the difference between the classification accuracy of the four health conditions while improving the accuracy, and the overall accuracy reaches the maximum value, avoiding the impact of information differences in the original data on classification, and is more able to mine the deep information behind the fault features.

For the CNN model with the original vibration signal, the diagnostic accuracy is high and close to the algorithm proposed in this paper. However, since this paper is oriented to the aviation field, according to the guidance for vibration-based diagnostic algorithms in ADS-79D-HDBK, "the designed condition indicator behavior should be firmly based on the physics of failure character of the device or system." Due to the black-box effect, the CNN model is difficult to apply in the aviation field, where the classification model based on feature engineering is preferred.

Table 3: Comparison of classifiers.

	CH accuracy (%)	CI accuracy (%)	CO accuracy (%)	CB accuracy (%)	Overall accuracy (%)
RF (in this paper)	96.67	**100**	**100**	95	**97.92**
AdaBoost	89.17	97.50	93.33	86.67	91.67
BPNN	80.00	95.00	72.50	95.83	85.83
DA	83.33	96.67	88.33	77.50	86.46
DT	91.67	99.17	91.67	79.17	90.42
GMM	70.00	100	98.33	93.33	90.42
KNN	94.17	99.17	90.83	95.00	94.79
NB	84.17	97.50	92.50	91.67	91.46
SVM	90.83	100	95.83	95.00	95.42
CNN (with original vibration signal)	**99.50**	99.00	95.50	**97.00**	97.75
CNN (with filtered features)	91.50	98.25	91.50	83.75	91.25

6. Conclusion

To deal with the problem that the traditional bearing fault classification methods are not suitable for variable speed conditions, a novel feature of MSFDI is proposed, based on the effective time-frequency domain representation by FrFT and the availability of dimensionless indicators in FrFDs, which is combined with the ReliefF for selecting sensitive features and reducing the input features of the classifier while improving accuracy. The selected sensitive feature subset is inputted into RF for classification. Experiments show that the proposed method has outstanding performance with the average accuracy reaching 97.92%. Through comparisons of various aspects, including feature extraction methods, feature selection methods, and classifiers, the advantages of the proposed method can be effectively verified. In addition, although this method has greatly reduced the number of input features of the RF classifier, how to filter features further on the basis of the proposed method is worthy of further research.

Data Availability

The data used to support the findings of this study are available from the corresponding author upon request.

Conflicts of Interest

The authors declare that they have no conflicts of interest.

Acknowledgments

This work was supported by the National Natural Science Foundation of China (Grant no. 52075031) and the Central Funds Guiding the Local Science and Technology Development (Grant no. 206Z5001G).

References

[1] S. Zhang, Z. Liu, S. He, J. Wang, and L. Chen, "Improved double TQWT sparse representation using the MQGA algorithm and new norm for aviation bearing compound fault detection," *Engineering Applications of Artificial Intelligence*, vol. 110, Article ID 104741, 2022.

[2] G. Li, G. Tang, H. Wang, and Y. Wang, "Blind source separation of composite bearing vibration signals with low-rank and sparse decomposition," *Measurement*, vol. 145, pp. 323–334, 2019.

[3] J. Ma, S. Zhuo, C. Li, L. Zhan, and G. Zhang, "Study on noncontact aviation bearing faults and speed monitoring," *IEEE Transactions on Instrumentation and Measurement*, vol. 70, pp. 1–21, 2021.

[4] M. Yu, X. Pan, Z. Feng, and M. Fang, "A method to diagnose compound fault of rolling bearing with ITD-AF," *Journal of Vibroengineering*, vol. 23, no. 3, pp. 559–571, 2021.

[5] Z. Feng, X. Yu, D. Zhang, and M. Liang, "Generalized adaptive mode decomposition for nonstationary signal analysis of rotating machinery: principle and applications," *Mechanical Systems and Signal Processing*, vol. 136, Article ID 106530, 2020.

[6] V. Vakharia, V. K. Gupta, and P. K. Kankar, "Efficient fault diagnosis of ball bearing using ReliefF and Random Forest classifier," *Journal of the Brazilian Society of Mechanical Sciences and Engineering*, vol. 39, no. 8, pp. 2969–2982, 2017.

[7] H. Pan, Y. Yang, X. Li, J. Zheng, and J. Cheng, "Symplectic geometry mode decomposition and its application to rotating machinery compound fault diagnosis," *Mechanical Systems and Signal Processing*, vol. 114, pp. 189–211, 2019.

[8] J. Ben Ali, N. Fnaiech, L. Saidi, B. Chebel-Morello, and F. Fnaiech, "Application of empirical mode decomposition and artificial neural network for automatic bearing fault diagnosis based on vibration signals," *Applied Acoustics*, vol. 89, pp. 16–27, 2015.

[9] K. Dragomiretskiy and D. Zosso, "Variational mode decomposition," *IEEE Transactions on Signal Processing*, vol. 62, no. 3, pp. 531–544, 2014.

[10] Q. Hu, X. S. Si, A. S. Qin, Y. R. Lv, and Q. H. Zhang, "Machinery fault diagnosis scheme using redefined dimensionless indicators and mRMR feature selection," *IEEE Access*, vol. 8, Article ID 40313, 2020.

[11] G. Tang, Y. Wang, Y. Huang, L. Hiu, and J. He, "Compound bearing fault detection under variable speed conditions with virtual multi-channel signals in angle domain," *IEEE Transactions on Instrumentation and Measurement*, vol. 69, no. 8, pp. 5535–5545, 2020.

[12] L. B. Almeida, "The fractional Fourier transform and time-frequency representations," *IEEE Transactions on Signal Processing*, vol. 42, no. 11, pp. 3084–3091, 1994.

[13] D. Wang and K. L. Tsui, "Theoretical investigation of the upper and lower bounds of a generalized dimensionless bearing health indicator," *Mechanical Systems and Signal Processing*, vol. 98, pp. 890–901, 2018.

[14] J. Xiong, Q. Zhang, J. Wan, L. Liang, P. Cheng, and Q. Liang, "Data fusion method based on mutual dimensionless," *IEEE*, vol. 23, no. 2, pp. 506–517, 2018.

[15] A. Qin, Q. Hu, Y. Lv, and Q. Zhang, "Concurrent fault diagnosis based on Bayesian discriminating analysis and time series analysis with dimensionless parameters," *IEEE Sensors Journal*, vol. 19, no. 6, pp. 2254–2265, 2019.

[16] Q. Hu, X. S. Si, Q. H. Zhang, and A. S. Qin, "A rotating machinery fault diagnosis method based on multi-scale dimensionless indicators and random forests," *Mechanical Systems and Signal Processing*, vol. 139, Article ID 106609, 2020.

[17] J. Xiong, Q. Zhang, G. Sun, X. Zhu, M. Liu, and Z. Li, "An information fusion fault diagnosis method based on dimensionless indicators with static discounting factor and KNN," *IEEE Sensors Journal*, vol. 16, no. 7, pp. 2060–2069, 2016.

[18] Y. Wang, J. Zhao, C. Yang, and D. Xu, "Research on rolling bearing life prediction based on Pearson-KPCA multi-feature fusion," *Measurement*, vol. 201, Article ID 111572, 2022.

[19] B. Cui, Y. Weng, and N. Zhang, "A feature extraction and machine learning framework for bearing fault diagnosis," *Renewable Energy*, vol. 191, pp. 987–997, 2022.

[20] W. Zhao, Z. Zhang, and L. Wang, "Manta ray foraging optimization: an effective bio-inspired optimizer for engineering applications," *Engineering Applications of Artificial Intelligence*, vol. 87, Article ID 103300, 2020.

[21] A. Faramarzi, M. Heidarinejad, B. Stephens, and S. Mirjalili, "Equilibrium optimizer: a novel optimization algorithm," *Knowledge-Based Systems*, vol. 191, Article ID 105190, 2020.

[22] S. Li, H. Chen, M. Wang, A. A. Heidari, and S. Mirjalili, "Slime mould algorithm: a new method for stochastic optimization," *Future Generation Computer Systems*, vol. 111, pp. 300–323, 2020.

[23] Y. Zhang, Z. Jin, and S. Mirjalili, "Generalized normal distribution optimization and its applications in parameter extraction of photovoltaic models," *Energy Conversion and Management*, vol. 224, Article ID 113301, 2020.

[24] A. Faramarzi, M. Heidarinejad, S. Mirjalili, and A. Gandomi, "Marine Predators algorithm: a nature-inspired metaheuristic," *Expert Systems with Applications*, vol. 152, Article ID 113377, 2020.

[25] Y. Liu, C. Zhao, H. Liang, H. Lu, N. Cui, and K. Bao, "A rotor fault diagnosis method based on BP-Adaboost weighted by non-fuzzy solution coefficients," *Measurement*, vol. 196, Article ID 111280, 2022.

[26] J. Li, X. Yao, X. Wang, Q. Yu, and Y. Zhang, "Multiscale local features learning based on BP neural network for rolling bearing intelligent fault diagnosis," *Measurement*, vol. 153, Article ID 107419, 2020.

[27] Y. Zhou, S. Yan, Y. Ren, and S. Liu, "Rolling bearing fault diagnosis using transient-extracting transform and linear discriminant analysis," *Measurement*, vol. 178, Article ID 109298, 2021.

[28] V. Gunasegaran and V. Muralidharan, "Fault diagnosis of spur gear system through decision tree algorithm using vibration signal," *Materials Today Proceedings*, vol. 22, pp. 3232–3239, 2020.

[29] S. Cao, Z. Hu, X. Luo, and H. Wang, "Research on fault diagnosis technology of centrifugal pump blade crack based on PCA and GMM," *Measurement*, vol. 173, Article ID 108558, 2021.

[30] H. Kumar and S. Manjunath, "Use of empirical mode decomposition and K-nearest neighbour classifier for rolling element bearing fault diagnosis," *Materials Today Proceedings*, vol. 52, pp. 796–801, 2022.

[31] G. Tang, B. Pang, T. Tian, and C. Zhou, "Fault diagnosis of rolling bearings based on improved fast spectral correlation and optimized random forest," *Applied Sciences*, vol. 8, no. 10, p. 1859, 2018.

[32] S. Buchaiah and P. Shakya, "Bearing fault diagnosis and prognosis using data fusion based feature extraction and feature selection," *Measurement*, vol. 188, Article ID 110506, 2022.

[33] J. Gu, Y. Peng, H. Lu, X. Chang, and G. Chen, "A novel fault diagnosis method of rotating machinery via VMD, CWT and improved CNN," *Measurement*, vol. 200, Article ID 111635, 2022.

[34] V. Sinitsin, O. Ibryaeva, V. Sakovskaya, and V. Eremeeva, "Intelligent bearing fault diagnosis method combining mixed input and hybrid CNN-MLP model," *Mechanical Systems and Signal Processing*, vol. 180, Article ID 109454, 2022.

[35] J. Mei, J. D. Jia, R. Zeng, B. Zhou, and H. Zhao, "A multi-order FRFT self-adaptive filter based on segmental frequency fitting and early fault diagnosis in gears," *Measurement*, vol. 91, pp. 532–540, 2016.

[36] H. M. Ozaktas, O. Arikan, M. Kutay, and G. Bozdagt, "Digital computation of the fractional Fourier transform," *IEEE Transactions on Signal Processing*, vol. 44, no. 9, pp. 2141–2150, 1996.

[37] L. Sun, T. Yin, W. Ding, Y. Qian, and J. Xu, "Multilabel feature selection using ML-ReliefF and neighborhood mutual information for multilabel neighborhood decision systems," *Information Sciences*, vol. 537, pp. 401–424, 2020.

[38] S. Aouabdi, M. Taibi, S. Bouras, and N. Boutasseta, "Using multi-scale entropy and principal component analysis to monitor gears degradation via the motor current signature analysis," *Mechanical Systems and Signal Processing*, vol. 90, pp. 298–316, 2017.

[39] H. Huang and N. Baddour, "Bearing vibration data under time-varying rotational speed conditions," *Data in Brief*, vol. 2, 2019.

[40] H. Huang, N. Baddour, and M. Liang, "Multiple time-frequency curve extraction Matlab code and its application to automatic bearing fault diagnosis under time-varying speed conditions," *MethodsX*, vol. 6, pp. 1415–1432, 2019.